



# Edge electronic vacancy on ultrathin carbon nitride nanosheets anchoring O<sub>2</sub> to boost H<sub>2</sub>O<sub>2</sub> photoproduction

Lian-Lian Liu<sup>a</sup>, Fei Chen<sup>a,b,\*</sup>, Jing-Hang Wu<sup>a</sup>, Ming-Kun Ke<sup>a</sup>, Chao Cui<sup>a</sup>, Jie-Jie Chen<sup>a,\*\*</sup>, Han-Qing Yu<sup>a,\*\*</sup>

<sup>a</sup> CAS Key Laboratory of Urban Pollutant Conversion, Department of Environmental Science and Engineering, University of Science & Technology of China, Hefei 230026, China

<sup>b</sup> Key Laboratory of the Three Gorges Reservoir Region's Eco-Environment, Ministry of Education, College of Environment and Ecology, Chongqing University, Chongqing 400045, China

## ARTICLE INFO

### Keywords:

Electronic vacancy  
H<sub>2</sub>O<sub>2</sub> production  
Oxygen reduction  
Photocatalysis  
Selectivity

## ABSTRACT

The utilization of solar energy for hydrogen peroxide (H<sub>2</sub>O<sub>2</sub>) production using graphitic carbon nitride (g-C<sub>3</sub>N<sub>4</sub>) under visible light irradiation has attracted increasing interests due to its high efficiency and cost-effectiveness. However, this process is still limited by slow charge carrier migration. In this work, continuous regulation of band structure inside g-C<sub>3</sub>N<sub>4</sub> is obtained by defect engineering through gradient calcination. The H<sub>2</sub>O<sub>2</sub> production rate (4980 μmol g<sup>-1</sup> h<sup>-1</sup>) of nitrogen-defective g-C<sub>3</sub>N<sub>4</sub> is 18 times higher than that of pristine g-C<sub>3</sub>N<sub>4</sub>. The π\*<sub>C=N-C</sub> signals in X-ray absorption near-edge structure spectrum decline, indicating an increased N-defects. The N-defects with the electronic vacancies in the heptazine intensifies its light-harvesting on g-C<sub>3</sub>N<sub>4</sub> and also improve the selectivity of 2-electron O<sub>2</sub> reduction. A quantitative structure-activity relationship between N-defects and band structure is unveiled. This work offers an accessible strategy to design photocatalysts with desirable defect structures for energy conservation.

## 1. Introduction

Hydrogen peroxide (H<sub>2</sub>O<sub>2</sub>) is a versatile clean oxidant and widely used in organic synthesis, water, and wastewater purification, disinfection, pulp bleaching, etc [1]. Besides, H<sub>2</sub>O<sub>2</sub> is also a promising future solar fuel with an estimated energy density of 3.0 MJ L<sup>-1</sup> for 60 wt% H<sub>2</sub>O<sub>2</sub>, while the correspondent H<sub>2</sub> at 35 MPa compression contains only 2.8 MJ L<sup>-1</sup> [2]. Thus, compared to H<sub>2</sub>, H<sub>2</sub>O<sub>2</sub> is more efficient as another energy carrier candidate and easier to store and transport [3–5]. As for the applicative methods of H<sub>2</sub>O<sub>2</sub> production, the reaction of anthraquinone with O<sub>2</sub> is generally adopted, but this process has some severe drawbacks, such as high energy consumption, complicated industrial procedures, and toxic by-products as well as catalyst deactivation [6,7]. Another alternative strategy is the direct synthesis of H<sub>2</sub>O<sub>2</sub> with H<sub>2</sub> and O<sub>2</sub> using the noble metal-based catalysts under high temperatures and pressures, but it is limited by the potentially explosive nature of the H<sub>2</sub>/O<sub>2</sub> mixture [2]. Undoubtedly, an inexpensive and efficient approach capable of producing H<sub>2</sub>O<sub>2</sub> with relatively high yields is greatly desired.

The problems of producing H<sub>2</sub>O<sub>2</sub> by the above two common methods can be resolved by photocatalysis, which has been demonstrated to be a typical proton-coupled electron transfer (PCET) pathway. In this process, the photocatalysts initially absorb light energy and generate separated electrons and holes. Then, the photogenerated electrons can capture dissolved O<sub>2</sub> from water and react with the protons to boost H<sub>2</sub>O<sub>2</sub> via a one-step two-electron (Eq. (1)) or two-step continuous single-electron (Eqs. (2–4)) O<sub>2</sub> reduction [8]. However, the yield of H<sub>2</sub>O<sub>2</sub> is not high, possibly attributable to the low conversion efficiency of •O<sub>2</sub><sup>-</sup> to H<sub>2</sub>O<sub>2</sub> (Eqs. (3–4)). Besides, the competitive reactions such as the H<sub>2</sub> evolution reaction (HER, Eq. (5)) and four-electron O<sub>2</sub> reduction reaction (4e<sup>-</sup> ORR, Eq. (6)) also impede the H<sub>2</sub>O<sub>2</sub> production by reducing the selectivity of the 2e<sup>-</sup> O<sub>2</sub> reduction pathway [9,10]. Hence, the elaborate design of photocatalytic materials with both high activity and high 2e<sup>-</sup> selectivity is essential.



\* Corresponding author at: CAS Key Laboratory of Urban Pollutant Conversion, Department of Environmental Science and Engineering, University of Science & Technology of China, Hefei 230026, China.

\*\* Corresponding authors.

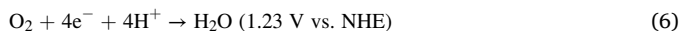
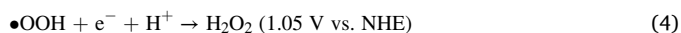
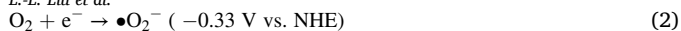
E-mail addresses: [fchen0505@cqu.edu.cn](mailto:fchen0505@cqu.edu.cn) (F. Chen), [chenjie@ustc.edu.cn](mailto:chenjie@ustc.edu.cn) (J.-J. Chen), [hqyu@ustc.edu.cn](mailto:hqyu@ustc.edu.cn) (H.-Q. Yu).

<https://doi.org/10.1016/j.apcatb.2021.120845>

Received 3 August 2021; Received in revised form 5 October 2021; Accepted 23 October 2021

Available online 28 October 2021

0926-3373/© 2021 Elsevier B.V. All rights reserved.



The star photocatalytic material  $\text{TiO}_2$  has been successfully used to produce  $\text{H}_2\text{O}_2$  in  $\text{O}_2$ -saturated water under UV light irradiation [11]. But the underutilization of solar energy, the rapid recombination of photo-generated electron-hole pairs ( $\text{e}^-/\text{h}^+$ ), and the poor selectivity for  $2\text{e}^-$   $\text{O}_2$  reduction are still the main stumbling blocks. Recently metal-free graphitic carbon nitride (g- $\text{C}_3\text{N}_4$ ) with a two-dimensional conjugated structure as a photocatalyst has attracted increasing interest since it was first reported by Wang et al. in 2009 [12]. Unfortunately, the efficiency of photocatalytic  $\text{H}_2\text{O}_2$  production with the pristine g- $\text{C}_3\text{N}_4$  was still unsatisfactory. The poor photoactivity may be assigned to the inherent disadvantages of g- $\text{C}_3\text{N}_4$  [13], such as the weak visible light absorption, high recombination rate of photo-generated electron-hole pairs, and low selectivity for  $2\text{e}^-$   $\text{O}_2$  reduction.

Thus, various approaches have been used to boost the  $\text{H}_2\text{O}_2$  yield and quantum efficiency of pristine g- $\text{C}_3\text{N}_4$ , e.g., morphological design [14], heterogeneous doping [15,16], molecular engineering [17,18], heterojunctions [19,20], and cocatalyst loadings [9]. Among these methods, defect engineering [21–24] can regulate the electronic structure of g- $\text{C}_3\text{N}_4$  to achieve efficient activation of molecular oxygen. Generally, the carbon or nitrogen-defects (N-defects) can be readily introduced into the g- $\text{C}_3\text{N}_4$  framework by alkali-assisted methods [23–25]. However, the emergence of impurity elements or cyano groups is inevitable, while the concentration of defects is also uncontrollable, which leads to uncertainties and difficulty in studying the intrinsic mechanism of photo-activity enhancement. On the other hand, the quantitative structure-activity relationships between defects and  $2\text{e}^-$   $\text{O}_2$  reduction kinetics have not been established. To resolve these problems, we propose a gradient calcination procedure to prepare the defect-rich g- $\text{C}_3\text{N}_4$  under different atmospheres. This method allows an accurate introduction of a single type of defect and the controllable concentration in the g- $\text{C}_3\text{N}_4$  framework. The N-defective g- $\text{C}_3\text{N}_4$  obtained by high-temperature treatment of pristine g- $\text{C}_3\text{N}_4$  under an inert atmosphere can avoid the above-mentioned problems, and thus is a model to

study the structure-activity relationship between defects and  $2\text{e}^-$   $\text{O}_2$  reduction [26,27].

In this work, the g- $\text{C}_3\text{N}_4$  ultra-thin nanosheets with various defect concentrations were prepared by using a multi-step calcination method under different atmospheric conditions (Scheme S2, in the Supporting Information). The variations of visible-light-harvesting capacity and the transfer kinetics of photo-generated charges were investigated by the combinations of experimental investigations and theoretical calculations. The relationship between  $\text{O}_2$  adsorption capacity and the evolution of  $\text{H}_2\text{O}_2$  causing by the generation of N defects with the electronic vacancies was also tentatively unveiled. Our work provides a cost-effective strategy to tailor the defect structure of g- $\text{C}_3\text{N}_4$  for “solar-to-energy” conversion.

## 2. Experimental procedures

### 2.1. Synthesis

Bulk g- $\text{C}_3\text{N}_4$  (denoted as CN) was synthesized by thermal polymerization [28]. Typically, 10 g of melamine was put into a crucible with a lid, transferred into a muffle furnace, heated to  $550^\circ\text{C}$  at a heating rate of  $2.5^\circ\text{C min}^{-1}$ , and stabilized for 4 h. After cooling down to room temperature, the yellow CN was ground and collected for the subsequent experiments. The g- $\text{C}_3\text{N}_4$  nanosheets (CNS) were prepared by a simple thermal exfoliation method. Briefly, 0.5 g of CN powder was evenly dispersed in an open crucible and calcined at  $520^\circ\text{C}$  for 4 h at a heating rate of  $2.5^\circ\text{C min}^{-1}$ . Finally, the white CNS powders were obtained. To introduce N-defects, the as-prepared CNS powders were calcined again under  $\text{N}_2$  atmosphere. In a typical synthesis, the CNS powders were placed in a tube furnace and calcined at different temperatures with a ramping rate of  $2.5^\circ\text{C min}^{-1}$  for 2 h. The obtained samples were denoted as CNS-X (X = 400, 500, 600, and 650 correspond to the calcination temperatures of 400, 500, 600, and  $650^\circ\text{C}$ ).

### 2.2. Characterizations

The X-ray diffractometer (XRD) patterns were obtained by a Philips X'Pert PRO SUPER X-ray diffractometer with  $\text{Cu K}\alpha$  radiation at 40 kV and 40 mA. The field emission scanning electron microscope (SEM) (Hitachi S-4800) and transmission electron microscopy (TEM) with a

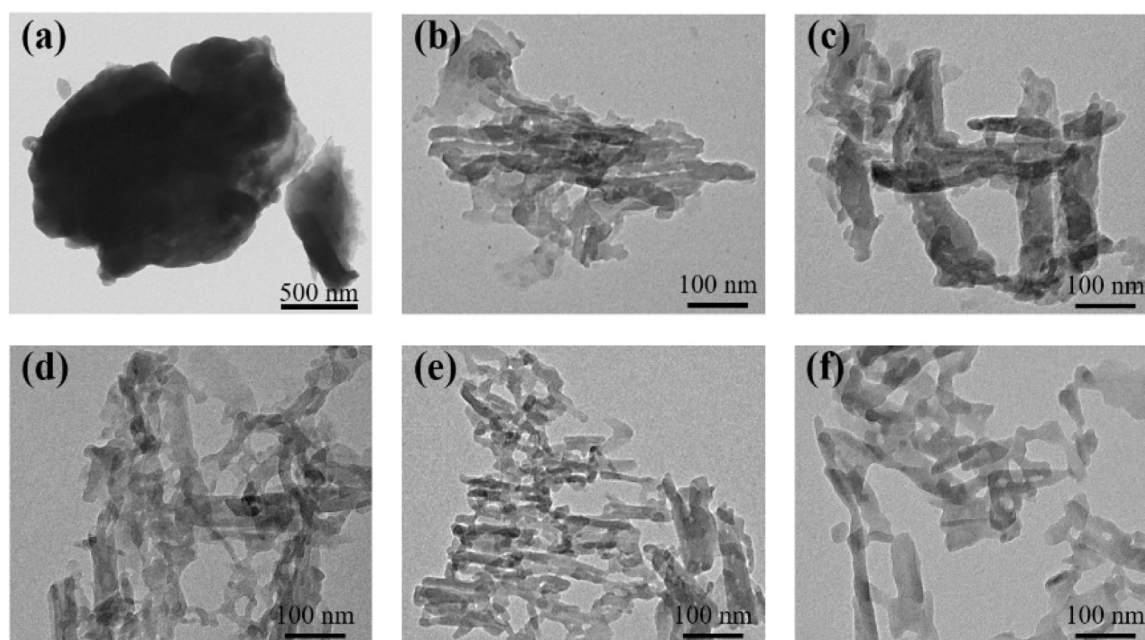
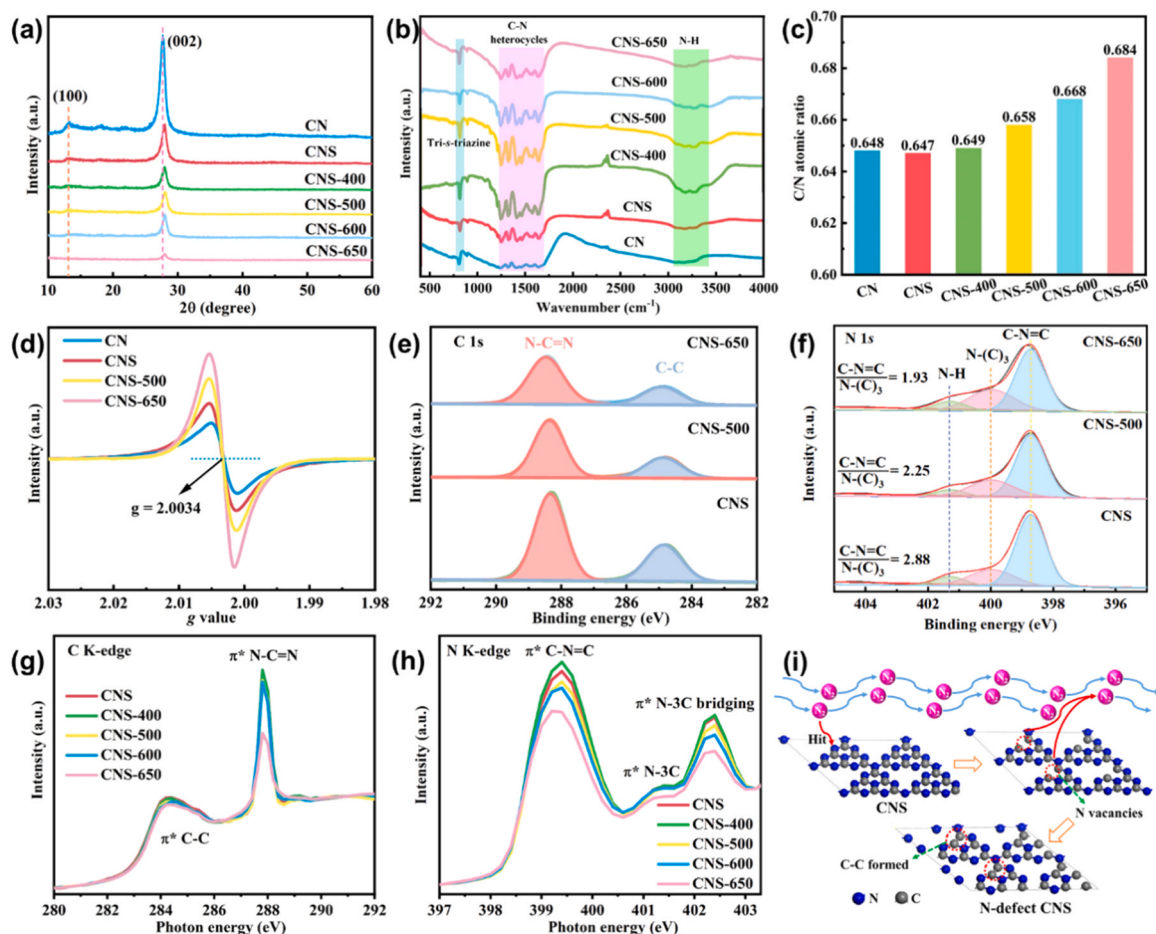


Fig. 1. TEM images of (a) CN, (b) CNS, (c) CNS-400, (d) CNS-500, (e) CNS-600, and (f) CNS-650.



**Fig. 2.** (a) XRD patterns, (b) FTIR spectra, (c) elemental analysis, (d) room-temperature ESR spectra, (e) C 1s and (f) N 1s high-resolution XPS spectra, (g) C K-edge and (h) N K-edge XANES of the prepared photocatalysts. (i) Proposed formation mechanism of nitrogen-defects in carbon nitride.

FEI Tecnai G20 were used to analyze the surface morphology. The thickness of the prepared photocatalysts was measured by a SmartSPM-1000 atomic force microscope (AFM). The surface properties of the samples were measured on a Fourier transform infrared spectroscopy (FTIR, Vertex 70, Bruker Co., Germany). The UV–vis diffuse reflectance spectrum (UV–vis DRS) was conducted in a UV-3700 spectrometer at the range of 250–800 nm. The valence states of the constituent elements were characterized by X-ray photoelectron spectroscopy (XPS) using a Thermo ESCALAB 250 spectrometer. The C L-edge and N L-edge X-ray absorption near-edge structure (XANES) spectra were recorded on the BL12B beamline at the National Synchrotron Radiation Laboratory in Hefei, China. The photoluminescence (PL) and time-resolved PL spectra were obtained by a FLS980 fluorescence spectrometer. Electron spin resonance (ESR) signals were recorded with an ESR spectrometer (ER200-SRC, Bruker Co., USA) at room temperature. Other characterizations were described in the [Supporting Information](#).

### 2.3. Photocatalytic activity evaluation

The photocatalytic production of  $\text{H}_2\text{O}_2$  was conducted at 25 °C with a circulating water system. A 300 W Xenon lamp (PLS-SXE 300D/300DUV, Beijing Perfectlight) with a 400 nm cutoff filter was used as the light source. The photocatalytic system contained 0.2 g  $\text{L}^{-1}$  of the prepared catalyst and 10 vol% of isopropanol. Before the reaction, the suspension was stirred in the dark for 15 min to reach an adsorption-desorption equilibrium. The concentration of  $\text{H}_2\text{O}_2$  was analyzed by the standard iodometric method [29]. The apparent quantum yield (AQY) for  $\text{H}_2\text{O}_2$  production was calculated by the equation of  $\text{AQY} =$

$$\frac{(\text{Number of produced } \text{H}_2\text{O}_2 \text{ molecules}) \times 2}{\text{Number of incident photons}} \times 100\%.$$

### 2.4. Density functional theory (DFT) calculations

The geometry optimizations, band structure, and density of electronic states calculations of the pristine and N-defective  $\text{g-C}_3\text{N}_4$  were performed using the CASTEP program package. In the computations, the exchange-correlation effects were described by the generalized gradient approximation (GGA), which was developed by Perdew, Burke, and Ernzerhof (PBE) [30,31]. Cut-off energy of 517 eV and a k-point set of  $4 \times 4 \times 2$  were used. The calculation accuracy was set to the total energy converges to  $1 \times 10^{-5} \text{ eV atom}^{-1}$  and the convergence criterion of the force between atoms was  $0.03 \text{ eV } \text{\AA}^{-1}$ . The maximum displacement was  $1 \times 10^{-3} \text{ \AA}$  and the maximum stress was 0.05 GPa. Other calculation details are provided in the [Supporting Information](#).

## 3. Results and discussion

### 3.1. Formation of N-defects in $\text{g-C}_3\text{N}_4$

The surface morphology of the prepared photocatalysts was imaged by SEM and TEM. The pristine CN (Fig. 1a and S1a) presented as irregular blocks with a micro-range size. The two-dimensional CNS (Fig. 1b and S1b) were prepared by exfoliating the bulk CN. The CNS had an ultra-thin structure with a thickness of 1.56 nm (about 6 layers) (Fig. S2a) and an enlarged specific surface area of  $131.5 \text{ m}^2 \text{ g}^{-1}$ , which was much higher than that of CN ( $7.57 \text{ m}^2 \text{ g}^{-1}$ ) (Table S1). The designed CNS-X (X represents the re-calcination temperature in  $\text{N}_2$ )



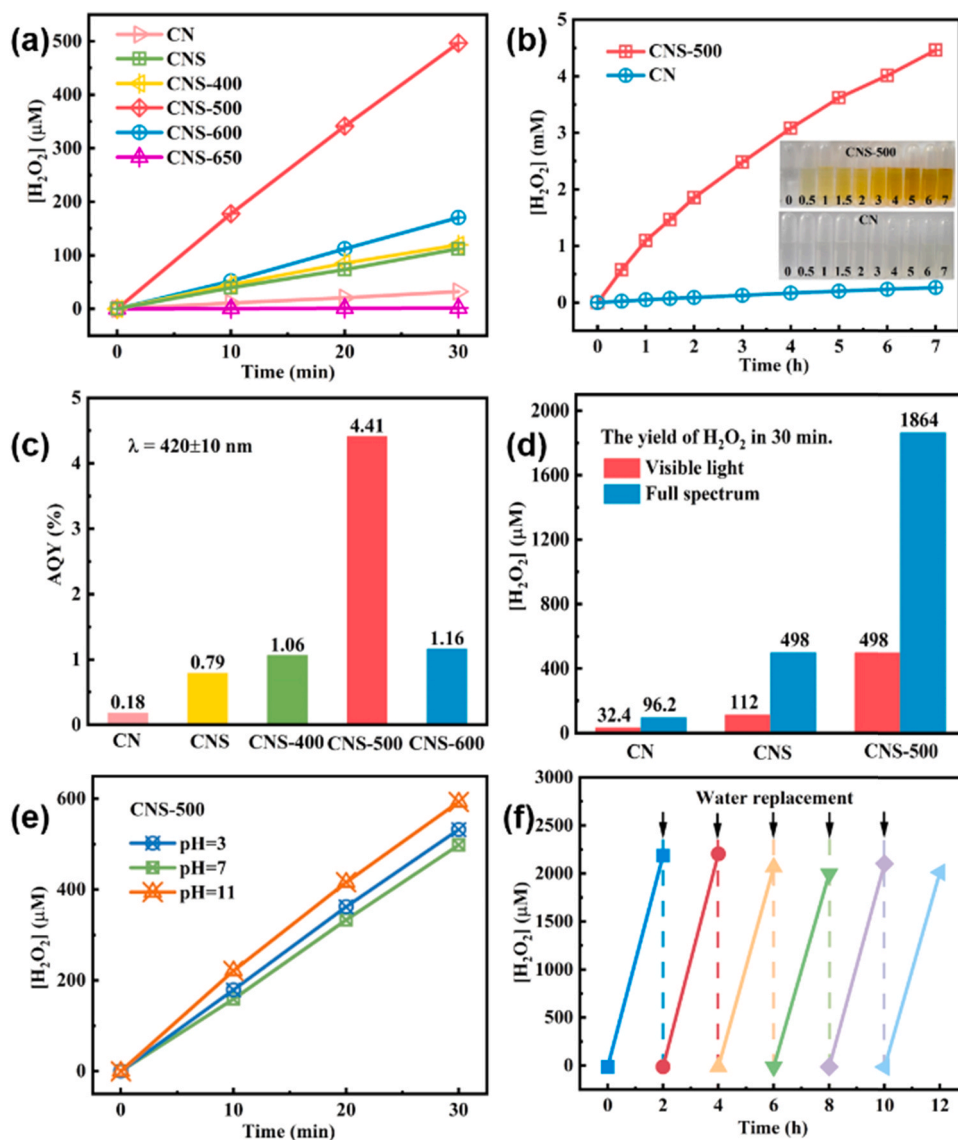


**Fig. 3.** (a) H<sub>2</sub>O<sub>2</sub> yields of the prepared photocatalysts under visible light irradiation ( $\lambda > 400$  nm). (b) The productions of H<sub>2</sub>O<sub>2</sub> with the prolonged reaction time. (c) The yields of H<sub>2</sub>O<sub>2</sub> under full-spectrum light irradiation. (d) AQY of the samples (irradiated by a 300 W Xe lamp using a  $420 \pm 10$  nm band-pass filters). (e) Effects of pH on H<sub>2</sub>O<sub>2</sub> production over CNS-500. (f) Stability test of CNS-500.

photocatalysts showed a thinner nanosheet structure (Fig. 1c,d and S1c, d) and the measured thicknesses of CNS-400, CNS-500, CNS-600, and CNS-650 were 0.76, 0.79, 0.76, and 0.51 nm, respectively (Fig. S2b–e) and the number of g-C<sub>3</sub>N<sub>4</sub> layers corresponded to 3, 3, 3, and 2 layers, respectively. Meanwhile, more adsorptive and catalytic sites were exposed because of the increased specific surface area after the second calcination, implying that a substantially enhanced photoactivity would be thus achieved.

The crystal structures of the products were measured by XRD. As shown in Fig. 2a, two typical diffraction peaks corresponding to g-C<sub>3</sub>N<sub>4</sub> were observed. The diffraction peak at  $27.5^\circ$  belonged to the interlayer stacking with the Miller index of (002) [32]. The diffraction peak at  $13.0^\circ$  was assigned to the in-plane structural packing motif, and the Miller index was (100) [33]. After the second calcination under the N<sub>2</sub> atmosphere, the diffraction peak of (002) shifted to a higher angle, which might be caused by the formation of defects in the g-C<sub>3</sub>N<sub>4</sub> framework. To further investigate the variations of functional groups after the stepwise calcination, FTIR spectra of all the photocatalysts were obtained (Fig. 2b). The sharp absorption band at  $810\text{ cm}^{-1}$  belonged to the heptazine unit [16], the characteristic peaks in the range

of  $1250\text{--}1700\text{ cm}^{-1}$  were attributed to the C–N heterocycle [34], and the signal at  $3300\text{ cm}^{-1}$  corresponded to the unpolymerized  $\text{—NH}_2$  group [35].

The atomic ratios of C/N of the as-prepared catalysts were evaluated by elemental analysis (Fig. 2c). The C/N atomic ratios of CN and CNS were consistent, indicating that no obvious chemical structural changes occurred at the thermal exfoliation step. However, the C/N atomic ratio increased from 0.658 (CNS-400) to 0.684 (CNS-650) when the secondary calcination temperature was elevated. Thus, the decline of the N atom fraction after the secondary calcination indicates that N-defects might be produced and the corresponding defect concentration could be adjusted by the secondary calcination temperature. The N defect-rich g-C<sub>3</sub>N<sub>4</sub> ultra-thin nanosheets with controllable defect levels could be easily obtained. Moreover, the formation of N-defects in CNS-X was also verified by the ESR analysis. CN exhibited a Lorentzian line centered at a g value of 2.00343 (Fig. 2d), which was attributable to the unpaired electrons in the  $\pi$ -conjugated tri-s-triazine unit [27]. The intensity order of the ESR signal was CNS-650 > CNS-500 > CNS, further validating that the level of N-defects was easily tunable.

XPS analyses were performed to detect the chemical state and



elemental content of the as-prepared photocatalysts. The high-resolution XPS spectra of C 1s (Fig. 2e and S3) could be divided into two peaks at 288.4 eV and 284.8 eV, referring to the N=C—N groups and the C—C groups (adventitious C impurity), respectively [36,37]. The N 1s spectra showed the binding energy peaks at 398.8, 400.2, and 401.3 eV (Fig. 2f), corresponding to C=N—C, N—(C)<sub>3</sub>, and unpolymerized N—H, respectively [2,34,35]. The ratios of C=N—C and N—(C)<sub>3</sub> were calculated to be 2.88, 2.25, and 1.93 for CNS, CNS-500, and CNS-650, respectively. The decrease in the corner N atoms (C=N—C) content indicates that the defects arose at the corner site [27], which coincided well with the above observation. These results suggest that the successful synthesis of the N-defective g-C<sub>3</sub>N<sub>4</sub> ultrathin nanosheets at designed concentrations was accomplished.

XANES spectra are useful to explore the local electronic and chemical structures. To further demonstrate the introduction of N-defects in the two-dimensional framework of CNS, C, and N K-edge XANES spectra were collected. The XANES C K-edge and N K-edge spectra indicate that the N-defective CNS-based catalysts retained the tri-s-triazine structure. In the C K-edge spectra (Fig. 2g), two peaks at around 284.3 eV and 287.8 eV could be observed for all samples, attributable to the  $\pi^*$  excitations of out-of-plane C—C and the in-plane N=C—N bonding [38,39]. A close study on the C K-edge spectra shows that the intensity of the  $\pi^*$  C—C feature decreased after the second calcination treatment. This might be assigned to the exfoliation effect of the host framework by nitrogen, which weakened the interlayer bonding of the CNS-X [40]. The decline in the intensity of the  $\pi^*$  N=C—N feature peak implies poor crystallinity or disordered chemical structure [41]. As displayed in Fig. 2g, the  $\pi^*$  N=C—N feature peak intensity of CNS-X gradually decreased with an increase in the second calcination temperature. This could be interpreted as the disruption of the N=C—N coordination structure with the introduction of N-vacancies, resulting in a severe structural disorder in the  $sp^2$  plane. The N K-edge XANES spectra (Fig. 2h) also confirm the formation of N-defects with three main features belonging to the  $\pi^*$  excitations of in-plane C=N—C bonds (ca. 399.4 eV), N—3C bonds (ca. 401.4 eV), and  $sp^3$  N—3C bridging (ca. 402.4 eV) between tri-s-triazine units [42]. As the second calcination temperature was elevated, the intensity of the  $\pi^*$  C=N—C feature peak gradually decreased, implying an increase in the concentration of N-defects. This result is in line with the XPS detection results. However, the intensity of the  $\pi^*$  N<sub>3</sub> C peak slightly decreased, which might be due to the formation of N-defects and lead to the partial destruction of the N-3C bond in the CNS framework [43]. These results indicate that the C=N—C coordination structure became decomposed after the second high-temperature treatment, whereby N-defects were formed and the level of N-defects depended on the calcination temperature.

The possible formation mechanism of N-defects was proposed (Fig. 2i) [26]. The internal energy of N<sub>2</sub> molecules increased with the elevated temperatures and their irregular motion intensified. When the N<sub>2</sub> molecules with high kinetic energy could attack N atoms on the surface of the g-C<sub>3</sub>N<sub>4</sub> ultra-thin nanosheets, the specific energy transfer to the target atoms occurred. When the energy received by the target N atom was higher than the binding energy of C=N—C, the N atom could be sputtered from the surface of the material and N vacancy was thus formed. Compared with the bridging or center N atoms, the less stable corner N atoms at the edge of heptazine might be more likely to be sputtered out and form defects in the calcination. To verify this assumption, the formation energy of N-defect in g-C<sub>3</sub>N<sub>4</sub> was also calculated (Fig. S4). The formation energy of N-defect ( $\Delta E$ ) decreased from positive to negative values with an increased temperature. This result indicates that high temperature was beneficial to the formation of N-defects, which is in good agreement with the experimental results.

### 3.2. Photocatalytic performance of H<sub>2</sub>O<sub>2</sub> production

The photocatalytic performance of the prepared photocatalysts was evaluated by measuring the yield of H<sub>2</sub>O<sub>2</sub> under visible light

( $\lambda > 400$  nm) within a certain period of irradiation time. The pristine CN generated a low amount of 28  $\mu\text{mol L}^{-1}$  H<sub>2</sub>O<sub>2</sub> within 30 min (Fig. 3a). The small specific surface area, narrow light absorption range and rapid recombination rate of photo-generated carriers were the main reasons. The CNS produced 112  $\mu\text{mol L}^{-1}$  of H<sub>2</sub>O<sub>2</sub> under identical conditions, which was attributed to the enhanced specific surface area after the thermal exfoliation process. After the successful introduction of N-defects in the secondary calcination, the selective H<sub>2</sub>O<sub>2</sub> production was substantially enhanced. For instance, the H<sub>2</sub>O<sub>2</sub> production of CNS-500 reached 498  $\mu\text{mol L}^{-1}$ , which was 18-fold higher than that of pure CN. In the appropriate temperature range ( $< 500$  °C) in the preparation process, an increase in N-defects led to an increase in H<sub>2</sub>O<sub>2</sub> production. However, when the temperature exceeded 500 °C, the detrimental effect of regenerative recombination centers might reduce the photocatalytic performance. Thus, there might be a structure-activity relationship between the amounts of defects amount and H<sub>2</sub>O<sub>2</sub> yield. Generally, when the defect concentration was controlled in an appropriate range, it could facilitate the light-harvesting capacity, charge mobility, and photocatalytic performance. Meanwhile, the introduction of N-defects might regulate the electronic structure of the heptazine unit, which further affected the selectivity of H<sub>2</sub>O<sub>2</sub> production. Moreover, the decomposition of H<sub>2</sub>O<sub>2</sub> on all the CNS materials was negligible (Fig. S6). Since g-C<sub>3</sub>N<sub>4</sub> with the poor H<sub>2</sub>O<sub>2</sub> adsorption ability had a moderate oxidation capacity of the photogenerated holes, the oxidation and decomposition of H<sub>2</sub>O<sub>2</sub> were thus inhibited [36,44]. Therefore, the CNS material could be designed as a catalyst for the production of H<sub>2</sub>O<sub>2</sub>.

After a prolonged irradiation experiment, the phototolerance of pristine CN and CNS-500 was investigated. The H<sub>2</sub>O<sub>2</sub> production of the CNS-500 reached 4.46 mmol L<sup>-1</sup> after 7 h light exposure (Fig. 3b). More H<sub>2</sub>O<sub>2</sub> might be generated when continuously prolonging the reaction time, suggesting that the CNS-500 exhibited an optically stable and satisfactory photoactivity. Moreover, the H<sub>2</sub>O<sub>2</sub> yield of the CNS-500 increased from 498 to 1864  $\mu\text{mol L}^{-1}$  within 30 min when the visible light irradiation was changed to full-spectrum light irradiation (Fig. 3c), further confirming its application prospects. Fig. 3d shows the AQY of pure CN and N-defective CN under monochromatic light irradiation ( $\lambda = 420 \pm 10$  nm). The AQE of the CNS-500 was estimated to be 4.41%, which was 25-fold higher than that of pure CN (0.18%), indicating that the CNS-500 could achieve efficient utilization of photo-generated electrons. A comparison with the previous related photocatalytic materials (Table S3) shows that the CNS-500 displayed outstanding superiorities in terms of cost input, reaction conditions, and H<sub>2</sub>O<sub>2</sub> generation rate.

The environmental adaptability of the CNS-500 at different catalyst dosages, pHs, ionic strengths, and various sacrificial agents was investigated. The yield of H<sub>2</sub>O<sub>2</sub> was substantially enhanced with the increasing catalyst dosage, and a good linear relationship was found between the yield of H<sub>2</sub>O<sub>2</sub> and catalyst amount (Fig. S7). No obvious variations of H<sub>2</sub>O<sub>2</sub> production (Fig. 3e) were found under acidic, neutral, and alkaline conditions, indicating its environmental tolerance. Notably, a slight increase in H<sub>2</sub>O<sub>2</sub> production might be caused by the increased ionic strength in the photocatalytic system. To verify this hypothesis, K<sub>2</sub>SO<sub>4</sub> was used to adjust the ionic strength of the reaction solution. The H<sub>2</sub>O<sub>2</sub> evolution enhanced with the increase in ionic strength in the reaction (Fig. S8). To achieve efficient H<sub>2</sub>O<sub>2</sub> production, sacrificial agents such as small organic molecules were synchronously added to provide protons and consume holes, further favoring the activation of molecular oxygen. The commonly used organic molecules such as methanol, ethanol, isopropanol, and oxalic acid were adopted. After these additives, the H<sub>2</sub>O<sub>2</sub> yields could all reach 500  $\mu\text{mol L}^{-1}$  (Fig. S9). Photocatalytic stability is another important index to evaluate future applications. As shown in Fig. 3f, the photocatalytic performance remained stable and the recovery of H<sub>2</sub>O<sub>2</sub> yield could remain at a higher level. Fig. S10 shows the comparison of the XPS spectra of the fresh and used CNS-500, and both spectra were almost identical, especially the retention of N-defects after the reaction. These results indicate that the

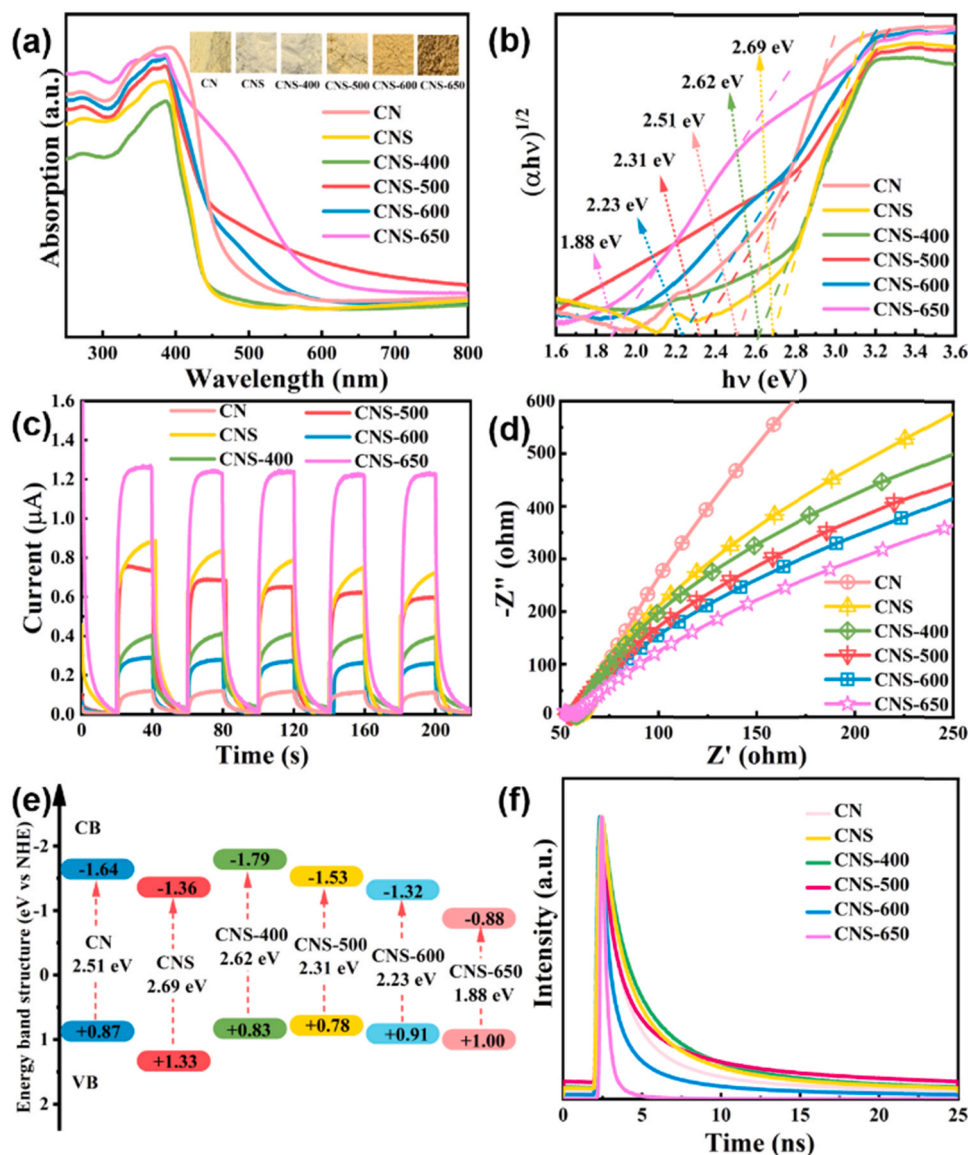


**Fig. 4.** (a) UV-vis diffuse reflectance spectra (the inset is the digital images of different photocatalysts), (b) corresponding plots of transformed Kubelka-Munk function versus photon energy, (c) transient photocurrent response curves, (d) Nyquist impedance plots, (e) energy band structure diagram, and (f) time-resolved PL decay spectra of the prepared photocatalysts.

CNS-500 had the long-term photocatalytic  $\text{H}_2\text{O}_2$  production capacity under visible light irradiation.

### 3.3. Structure-activity relationship

The excellent  $\text{H}_2\text{O}_2$ -producing activity of the CNS-500 might be ascribed to the optimization of the electronic structure after introducing a reasonable level of N-defects in the tri-s-triazine unit. UV-vis diffuse reflectance spectrum (UV-vis DRS) was used to explore the light-harvesting capacity of the prepared photocatalysts (Fig. 4a). The light absorption edge of CN was located at  $\sim 494$  nm, while the absorption edge of CNS was shifted to  $\sim 461$  nm owing to the quantum size effect [31]. After the second calcination of CNS at different temperatures, the obtained CNS-X showed the varying degrees of redshift and the wider spectral of solar light could be harnessed when gradually increasing secondary calcination temperature. Fig. 4b shows the correspondence between the transformed Kubelka-Munk function and photon energy [37]. The bandgap ( $E_g$ ) energies of CNS-X decreased with the increased N-defect level (or calcination temperature), and the correspondent  $E_g$

values of the CNS-400, CNS-500, CNS-600, and CNS-650 were estimated to be 2.62, 2.31, 2.23, and 1.88 eV, respectively. The positive slopes of Mott-Schottky curves (Fig. 5) indicate that all samples were n-type semiconductors [18,45]. For a n-type semiconductor, the conduction band potential ( $E_{\text{CB}}$ ) is 0.1 eV below flat band potential ( $E_{\text{FB}}$ ) [25]. The valence band potential ( $E_{\text{VB}}$ ) could be calculated by the following formula (Eq. (7)):

$$E_{\text{VB}} = E_g + E_{\text{CB}} \quad (7)$$

The  $E_{\text{VB}}$  values of the CNS-X were calculated to be 0.83, 0.78, 0.91, and 1.00 eV, respectively, while the corresponding  $E_{\text{CB}}$  values were  $-1.79$ ,  $-1.53$ ,  $-1.32$ , and  $-0.88$  eV (Fig. 4e). For the CNS-X, the  $E_{\text{CB}}$  values were more negative than the oxygen reduction potential ( $-0.33$  eV, Eq. (2)). Thus, the reduction of molecular oxygen could easily occur and further favor the generation of  $\bullet\text{O}_2^-$ .

The dependence of the bandgap on the N-vacancy level of CNS was further confirmed by DFT calculations. A series of CNS-based catalyst models with different N-defect levels were established to simulate the synthesized N-defect CNS. As shown in Fig. 6a-d, the pristine g-C<sub>3</sub>N<sub>4</sub>

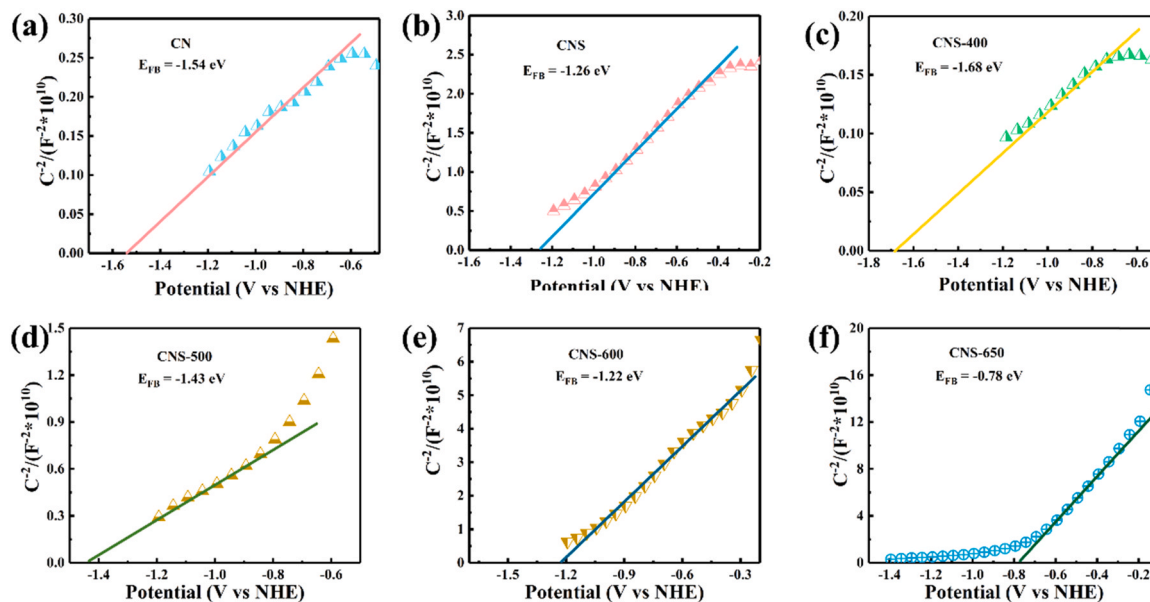


Fig. 5. Mott-Schottky plots of CN (a), CNS (b), CNS-400 (c), CNS-500 (d), CNS-600 (e), CNS-650 (f).

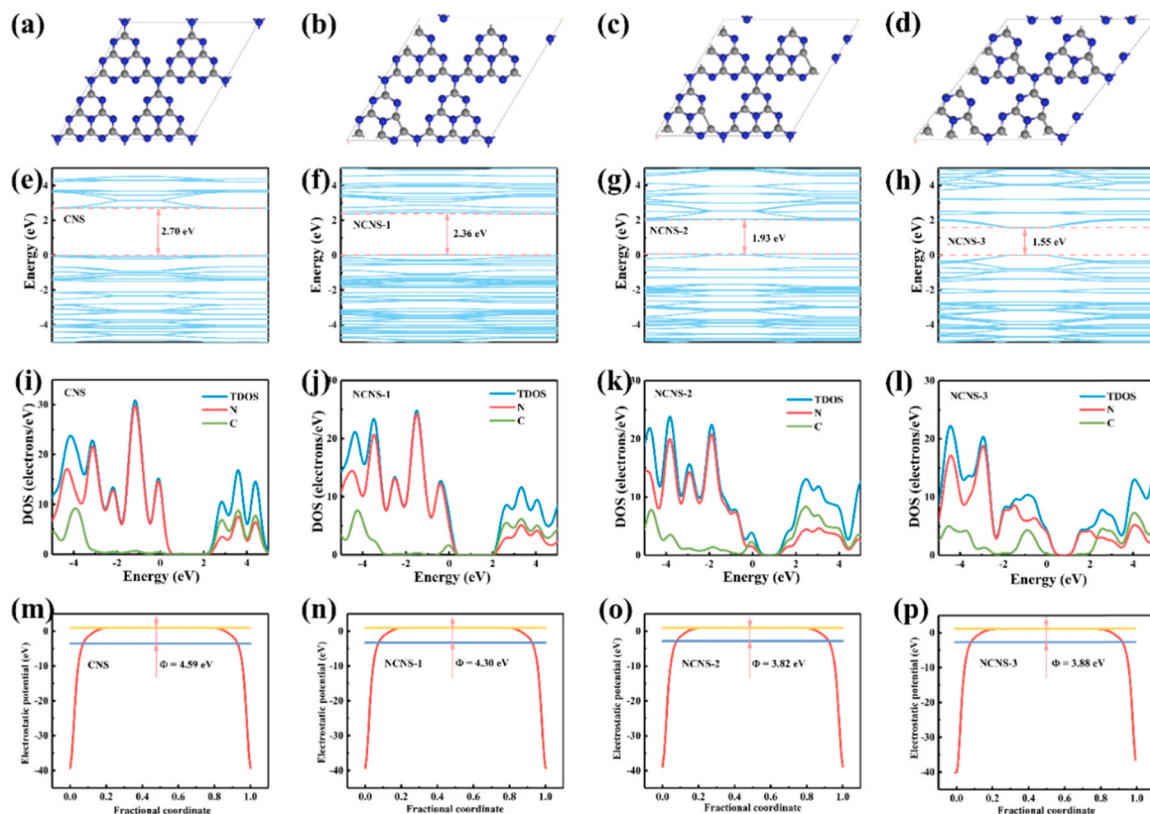


Fig. 6. Optimized geometry (a, b, c, d), band structure (e, f, g, h), DOS (i, j, k, l), and work function (m, n, o, p) of CNS, CNS-1, CNS-2, and CNS-3.

nanosheets were denoted as CNS, and CNS-1, CNS-2, CNS-3 referred g-C<sub>3</sub>N<sub>4</sub> nanosheets with a gradually increasing concentration of N-defects. The bandgap values of CNS, CNS-1, CNS-2, and CNS-3 had the calculated band gap values of 2.70, 2.36, 1.93, and 1.55 eV, respectively (Fig. 6e–h), and shrank with the increased defect number in the models, which agrees well with the experimental results. For pure CNS, the valence band (VB) edge consisted of 2p orbitals of N atoms, while the conduction band (CB) edge was mainly contributed by 2p orbitals of C atoms (Fig. 6i). The CNS with low N-defect concentration (CNS-1) has

similar VB and CB compositions (Fig. 6j) to pure CNS. However, the proportion of C 2p orbitals in the VB composition of CNS rose after increasing the N-defect concentration (CNS-2 and CNS-3, Fig. 6k,l). Such calculation results imply that it was feasible to achieve continuous regulation of the CNS bandgap by controlling the calcination temperature to tune the N-defect level.

The mobility and separation efficiency of photogenerated charges in the two-dimensional conjugate plane of CNS are also crucial factors governing its photocatalytic activity. Fig. 4c shows the transient



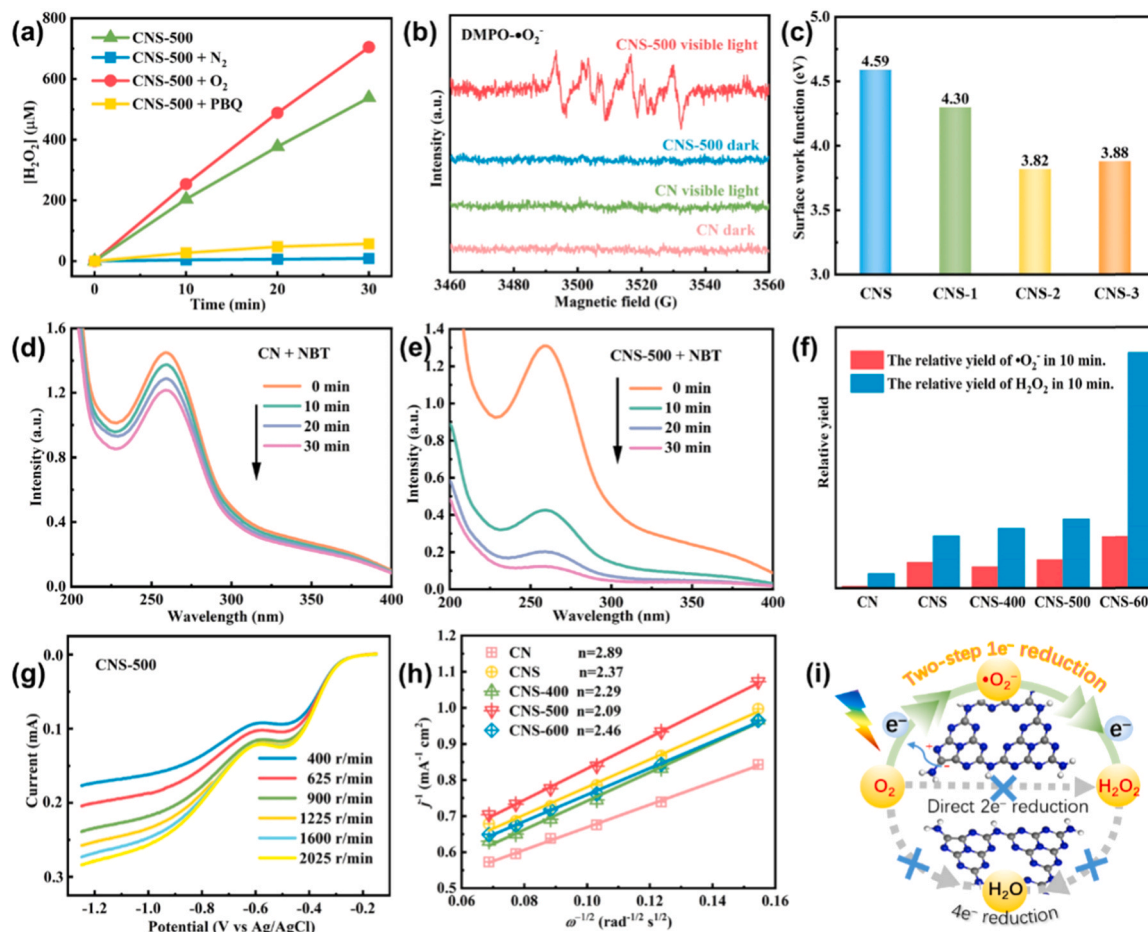


**Fig. 7.** (a) The effect of adding p-benzoquinone as a scavenger or blowing  $N_2/O_2$ /air on the production of  $H_2O_2$ . (b) EPR spectra of CN and CNS-500 with DMPO in methanol under dark conditions or visible light irradiation. (c) Surface work functions of CNS and N-defect CNS. The absorption intensity of NBT at 259 nm in (d) CN or (e) CNS-500 reactions solution. (f) Relative yields of  $H_2O_2$  and  $\bullet O_2^-$  of the catalysts. (g) LSV curves of CNS-500 at different speeds. (h) Koutecky-Levich plots of the ORR data measured by RDE analysis. (i) Schematic of  $H_2O_2$  formation mechanism.

photocurrent responses without bias under visible light irradiation. The CNS-650 prepared by the secondary calcination of CNS at  $650^\circ C$  exhibited the highest photocurrent, which was 12-fold higher than that of pristine CN. This result suggests that the N-defect-rich CNS could rapidly transfer the photoinduced electrons to participate in the redox reactions. Additionally, the electrochemical impedance spectroscopy (EIS) analysis was also performed to reflect the charge migration behaviors. Compared with pristine CN and CNS, all EIS Nyquist spectra (Fig. 4d) of CNS-X photocatalysts show a smaller arc diameter, suggesting a lower charge transfer resistance [46]. Thus, the introduction of N-defects could further weaken the charge transfer resistance of CNS and accelerate the transfer efficiency of the internal charge. The PL spectra (Fig. S5) can visualize the recombination of photogenerated electron-hole pairs [47]. The CNS-500 exhibited a weaker PL intensity, implying that a higher carrier separation efficiency was achieved under the secondary calcination at  $500^\circ C$ . The lifetimes of photo-generated carriers were investigated by the time-resolved PL decay spectra (Fig. 4f). The curves were fitted to the biexponential equations (Eqs. (8–9)):

$$R(t) = A_1 \exp(-t/\tau_1) + A_2 \exp(-t/\tau_2) \quad (8)$$

$$\tau_{ave} = (A_1 \times \tau_1^2 + A_2 \times \tau_2^2) / (A_1 \times \tau_1 + A_2 \times \tau_2) \quad (9)$$

where  $A_1$  and  $A_2$  are the pre-exponential factors,  $\tau_1$  and  $\tau_2$  indicate the long and short fluorescent lifetime. The average lifetime of pristine CN was 3.56 ns and increased to 4.01 ns for CNS. After the secondary calcination, the average lifetimes of CNS-500 and CNS-650 became 4.82

and 0.74 ns (Table S2), respectively.

Besides, the molecular orbital distribution of N-defect CNS can also reflect the separation performance of photogenerated carriers. The effects of N-defect on the distribution of the highest occupied molecular orbitals (HOMOs) and the lowest unoccupied molecular orbitals (LUMOs) were also explored. For pristine CN (Fig. 9a), the HOMOs were mainly distributed on the N atoms, while LUMOs were mostly located on the C atoms. A uniform distribution of HOMOs and LUMOs would lead to a high recombination rate of photo-generated electron-hole pairs [18], resulting in a lower photoactivity. After introducing a suitable N-defect, the molecular orbital distribution of the heptazine unit changed substantially. For CNS-1 (Fig. 9b), LUMOs were anchored on the defective heptazine unit, while HOMOs centralized on N atoms away from the defect. The spatial separation of LUMOs and HOMOs in CNS-1 facilitated the separation of photoinduced carriers. Moreover, the increase in the contour of the isosurface also indicates that CNS-1 showed a higher redox activity. Nevertheless, with a high N-defect level (CNS-3), the distribution of HOMOs and LUMOs became uniform again (Fig. 9c), leading to the formation of new recombination centers and shortening of the photo-generated charge lifetime. This result is consistent with the time-resolved PL decay spectra result.

The experimental and theoretical results mutually corroborated with the following structure-activity relationships: (1) The bandgap of CNS was related to the level of N-defects, and the bandgap became narrowed as the N-defect concentration increased. (2) At a reasonable level, the presence of N-defects optimized the electronic structure of CNS, reduced

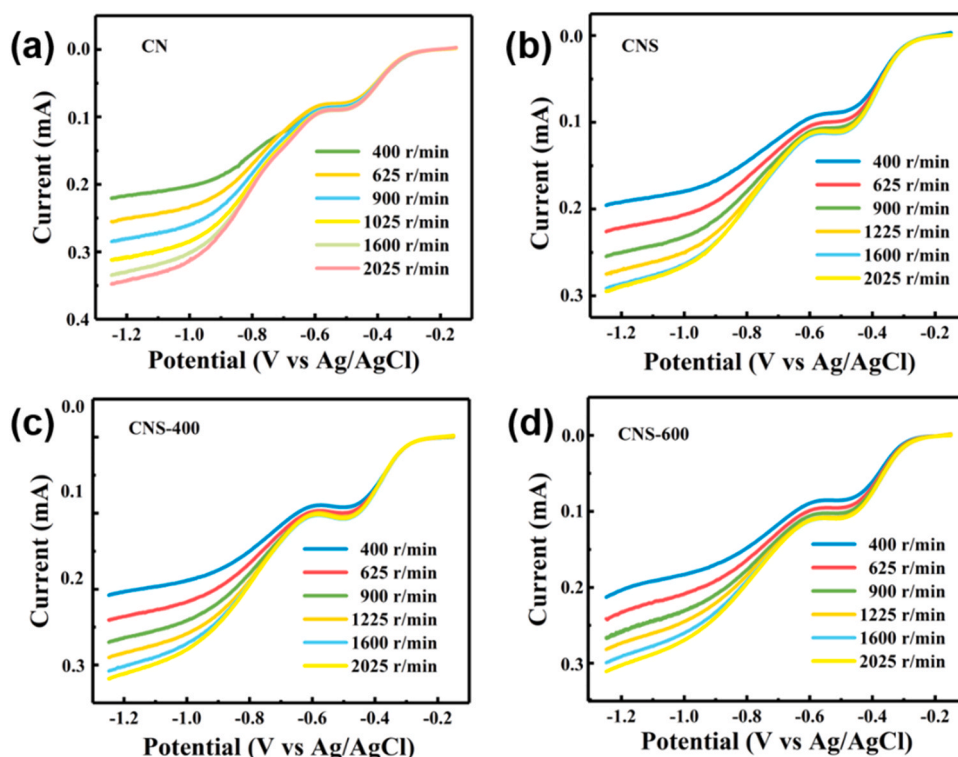


Fig. 8. LSV curves of CN (a), CNS (b), CNS-400 (c), and CNS-600 (d).

the charge transfer resistance, accelerated the charge mobility, prolonged the carrier lifetime, and improved the separation efficiency of electron-hole pairs. (3) However, when the N-defect level was too high, the charge transfer might be limited due to the formation of new recombination centers. Therefore, the CNS-500 exhibited the highest photocatalytic activity for  $\text{H}_2\text{O}_2$  generation due to its ability to generate more effective photogenerated electrons to participate in the  $\text{O}_2$  activation reaction.

### 3.4. $\text{H}_2\text{O}_2$ generation mechanism

The photocatalytic production of  $\text{H}_2\text{O}_2$  is reported as a two-step single-electron path ( $\text{O}_2 \rightarrow \bullet\text{O}_2^- \rightarrow \text{H}_2\text{O}_2$ ) or a one-step two-electron route ( $\text{O}_2 \rightarrow \text{H}_2\text{O}_2$ ) [4,48]. The source of oxygen in the oxygen reduction reaction was confirmed by blowing different gases into the reaction system. When compared with air, the  $\text{H}_2\text{O}_2$  production could be improved under  $\text{O}_2$  saturation conditions (Fig. 7a). Almost no  $\text{H}_2\text{O}_2$  evolution was observed under  $\text{N}_2$  saturation, suggesting that oxygen involved in the photocatalytic  $\text{O}_2$  reduction came from the dissolved molecular oxygen only. To further clarify the mechanism for  $\text{H}_2\text{O}_2$  production, the intermediate of  $\bullet\text{O}_2^-$  was recorded by 5,5-dimethyl-1-pyrroline N-oxide (DMPO) spin-trapping ESR technology [30]. Six characteristic peaks ascribed to DMPO- $\bullet\text{O}_2^-$  adducts were detected in the CNS-500 methanol suspension, while no visible DMPO- $\bullet\text{O}_2^-$  signal was found for CN under visible light irradiation (Fig. 7b). This result indicates that the formation of N-defects reinforced the transfer of photogenerated electrons to activate the molecular oxygen. The addition of *p*-benzoquinone (PBQ,  $\bullet\text{O}_2^-$  quencher) into the reaction system severely reduced the  $\text{H}_2\text{O}_2$  yield from 498 to 0  $\mu\text{mol L}^{-1}$ , implying that the formation of  $\text{H}_2\text{O}_2$  got through the two-step one-electron pathway only by CNS-500 and  $\bullet\text{O}_2^-$  was a crucial intermediate. Besides, the surface work function of CNS tended to decrease with the increasing defect level (Figs. 6m–p and 7c), indicating that the presence of N-defect was conducive to the escape of photo-generated electrons.

To further confirm the role of  $\bullet\text{O}_2^-$ , the nitroblue tetrazolium (NBT) transformation experiment was conducted to semi-quantitatively

determine the amount of  $\bullet\text{O}_2^-$  in the photocatalytic reaction (Fig. 7d,e and S13) [49]. The relative yields of both  $\bullet\text{O}_2^-$  and  $\text{H}_2\text{O}_2$  over different photocatalysts within 10 min are provided in Fig. 7f. The  $\text{H}_2\text{O}_2$  output was positively correlated with the  $\bullet\text{O}_2^-$  evolution, and the possible selective  $\text{H}_2\text{O}_2$  production pathway of  $\text{O}_2 \rightarrow \bullet\text{O}_2^- \rightarrow \text{H}_2\text{O}_2$  was reconfirmed. The CNS-500 exhibited a higher conversion efficiency from  $\bullet\text{O}_2^-$  to  $\text{H}_2\text{O}_2$ , demonstrating its higher selectivity with the proper N-defect level. Rotating disk electrode (RDE) analysis was also used to examine the number of electrons used for  $\text{O}_2$  reduction for all the photocatalysts [8]. The linear sweep voltammetry curves (LSV) of the photocatalysts at different rotation speeds are shown in Figs. 7g and 8. The first sharp step at  $-0.3$  V was attributed to the reduction reaction of  $\text{O}_2$  to  $\text{HO}_2^-$  [50], thus the two-step electron transfer mechanism was re-validated (Eqs. (2–4)). The Koutecky-Levich plots of the LSV data at  $-1.2$  V vs. Ag/AgCl are shown in Fig. 7h. The average number of electrons ( $n$ ) involved in the overall  $\text{O}_2$  reduction was determined by linear regression analyses with the slope of the plot. The  $n$  values for pristine CN, CNS, CNS-400, CNS-500, and CNS-600 were 2.89, 2.37, 2.29, 2.09, and 2.46, respectively. Especially, the  $n$  value for CNS-500 was closer to 2, indicating that the CNS-500 exhibited a higher output of  $\text{H}_2\text{O}_2$  and the N-defect could enhance the selectivity of two-step single-electron  $\text{O}_2$  reduction (Fig. 7i).

The above results show that the photocatalytic  $\text{H}_2\text{O}_2$  production by CNS-500 was controlled by the  $2e^-$   $\text{O}_2$  reduction. Thus, the  $\text{O}_2$  adsorption capacity of the different photocatalysts should be evaluated. The calculated adsorption energy of  $\text{O}_2$  on pristine CNS (Fig. 9d) was 0.22 eV. The adsorption energies of  $\text{O}_2$  at defect sites (Fig. 9e) and non-defect sites (Fig. 9f) in N-defect CNS were  $-0.69$  and  $-0.14$  eV, respectively. After the introduction of N-defects, the adsorption energy of  $\text{O}_2$  changed from positive to negative, indicating that the defects regulated the electron distribution and promoted the adsorption of  $\text{O}_2$ . Moreover, the adsorption energy of  $\text{O}_2$  at the defect site was more negative than that at the non-defective site, suggesting that the N-defect served as both adsorptive and activation sites for  $\text{O}_2$ , which was beneficial to the highly efficient production of  $\text{H}_2\text{O}_2$ .

Based on the above results, the possible mechanism for CNS-500 to

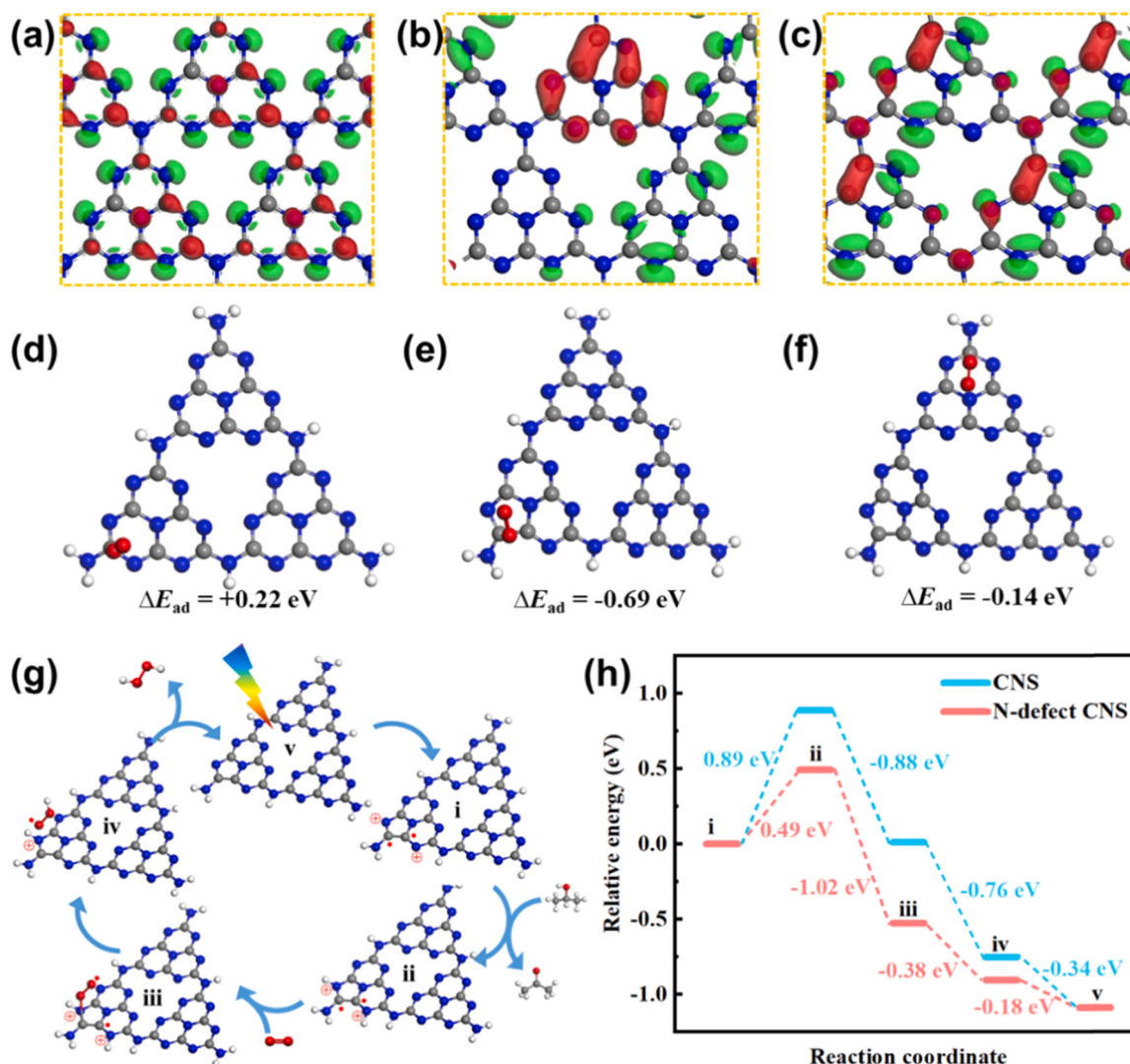


**Fig. 9.** HOMOs and LUMOs of (a) CNS, (b) CNS-1, and (c) CNS-3. Green and red represent the distribution of HOMOs and LUMOs, respectively. The adsorption configurations of  $\text{O}_2$  on (d) CNS, (e) defective sites of N-defect CNS, and (f) non-defective sites of N-defect CNS. (g) The mechanism of  $\text{H}_2\text{O}_2$  synthesis by N-defect CNS photocatalytic  $\text{O}_2$  reduction and (h) the relative energies of each step of  $\text{H}_2\text{O}_2$  production. (For interpretation of the references to color in this figure legend, the reader is referred to the web version of this article.)

photocatalytically reduce  $\text{O}_2$  to generate  $\text{H}_2\text{O}_2$  was proposed and is illustrated in Fig. 9g. The  $\text{H}_2\text{O}_2$  production in this photocatalytic system goes through the following steps: (1) The spatially separated electrons and holes are generated from N-deficient rich g- $\text{C}_3\text{N}_4$  under the excitation of visible light; (2) Isopropanol is oxidized by holes in the photocatalytic reactions to produce protons; (3) Oxygen is first adsorbed at the defect sites and then reacts with the photogenerated electrons; (4) One electron is transferred to  $\text{O}_2$  to form  $\bullet\text{O}_2^-$ , and the proton is coupled to form  $\bullet\text{OOH}$ ; (5) Another electron is transferred to  $\bullet\text{OOH}$ , and finally,  $\text{H}_2\text{O}_2$  is generated. The generation of  $\text{H}_2\text{O}_2$  in the above systems is a typical PCET process. In this process, the supply of protons and the activation of  $\text{O}_2$  are equally important, and both of them affect the production rate of  $\text{H}_2\text{O}_2$ . The variations of energy ( $\Delta E$ ) of the above reaction steps are shown in Fig. 9h. Except for the proton-producing reaction (Fig. 9g, i→ii) require additional energy injection, the other processes are all exothermic, indicating that the proton-producing reaction might determine the overall reaction rate. In other words, the formation of  $\text{H}_2\text{O}_2$  might be limited by the supply of protons. The introduction of N-defects reduces the  $\Delta E$  of the proton-producing reaction, which is beneficial to the generation of protons. Meanwhile, the defect sites could accelerate the adsorption and activation of  $\text{O}_2$ .

Therefore, the simultaneous improvement of proton supply and oxygen activation ability promotes the generation of  $\text{H}_2\text{O}_2$  via the PCET process.

#### 4. Conclusion

In summary, the g- $\text{C}_3\text{N}_4$  ultrathin nanosheets with various N-defect concentrations were successfully synthesized by using a gradient calcination method under different atmospheres. The multi-step calcination increased the specific surface area of g- $\text{C}_3\text{N}_4$  and enriched its pore structure. The formation of N-defects with the electronic vacancies strengthened the visible light absorption, accelerated charge transfer, and improved carrier separation efficiency. With the increase in defect level, the correspondent band gap gradually became narrower, which could further affect the photocatalytic activity. Appropriate levels of N-defects could achieve the spatial separation of HOMOs and LUMOs and inhibit the charge carrier recombination. The high selectivity of CNS-500 for photocatalytic production of  $\text{H}_2\text{O}_2$  was attributable to the fact that the defects could serve as both adsorptive and active sites of  $\text{O}_2$ . The yield of  $\text{H}_2\text{O}_2$  by CNS-500 under visible-light irradiation in 30 min could reach  $498 \mu\text{mol L}^{-1}$ , which was 18 times higher than that of pristine g- $\text{C}_3\text{N}_4$ . Moreover, CNS-500 had a good environmental tolerance and



recovery stability. Our work also shows that organic pollutants in practical wastewater could be applied as electron donors for photocatalytic production of  $\text{H}_2\text{O}_2$ , thus reducing the operational costs. Moreover, our work also provides insights into the structure-activity relationship between defect level and photocatalytic performance. The design principles outlined in this work might be also used for the controlled synthesis of highly efficient photocatalysts for energy conservation.

### CRedit authorship contribution statement

Lian-Lian Liu and Fei Chen conceived and planned the experiments and carried out the relative experiments. Lian-Lian Liu and Jie-Jie Chen contributed to the DFT calculations. Lian-Lian Liu conducted, and Fei Chen, Jing-Hang Wu, Ming-Kun Ke, and Chao Cui analyzed various characterizations. Lian-Lian Liu wrote the initial draft of the manuscript, and further modified by Fei Chen, Jie-Jie Chen and Han-Qing Yu.

### Declaration of Competing Interest

The authors declare that they have no known competing financial interests or personal relationships that could have appeared to influence the work reported in this paper.

### Acknowledgements

The authors thank the National Key R&D Program of China (2018YFC0406300), the National Natural Science Foundation of China (52027815, 51821006, 51978637, 51908528, and 52022093), the Fundamental Research Funds for the Central Universities (2021CDJQY-014), USTC Research Funds of the Double First-Class Initiative (YD3530002001), the Postdoctoral Innovation Talent Support Program of China (BX20180290), the China Postdoctoral Science Foundation (2018M640595), the Fundamental Research Funds for the Central Universities (WK2060120001), Youth Innovation Promotion Association, and the CAS Key Laboratory of Urban Pollutant Conversion Joint Research Fund (KLUPC-2020-3) for supporting this work. The soft X-ray absorption spectra were collected at the BL12B beamline in Hefei National Synchrotron Radiation Laboratory, China. The numerical calculations in this paper have been done on the supercomputing system in the Supercomputing Center of University of Science and Technology of China.

### Appendix A. Supporting information

Supplementary data associated with this article can be found in the online version at [doi:10.1016/j.apcatb.2021.120845](https://doi.org/10.1016/j.apcatb.2021.120845).

### References

- H.L. Hou, X.K. Zeng, X.W. Zhang, Production of hydrogen peroxide by photocatalytic processes, *Angew. Chem. Int. Ed.* 59 (2020) 2–23.
- Z. Teng, W. Cai, S. Liu, C. Wang, Q. Zhang, C. Su, T. Ohno, Bandgap engineering of polymeric carbon nitride copolymerized by 2,5,8-triamino-tri-s-triazine (melem) and barbituric acid for efficient nonsacrificial photocatalytic  $\text{H}_2\text{O}_2$  production, *Appl. Catal. B Environ.* 271 (2020), 118917.
- N. Kaynan, B.A. Berke, O. Hazut, R. Yerushalmi, Sustainable photocatalytic production of hydrogen peroxide from water and molecular oxygen, *J. Mater. Chem. A* 2 (2014) 13822–13826.
- J. Cai, J. Huang, S. Wang, J. Iocozzia, Z. Sun, J. Sun, Y. Yang, Y. Lai, Z. Lin, Crafting mussel-inspired metal nanoparticle-decorated ultrathin graphitic carbon nitride for the degradation of chemical pollutants and production of chemical resources, *Adv. Mater.* 31 (2019), 1806314.
- Y. Shiraishi, T. Takii, T. Hagi, S. Mori, Y. Kofuji, Y. Kitagawa, S. Tanaka, S. Ichikawa, T. Hirai, Resorcinol-formaldehyde resins as metal-free semiconductor photocatalysts for solar-to-hydrogen peroxide energy conversion, *Nat. Mater.* 18 (2019) 985–993.
- Z. Haider, H.I. Cho, G.H. Moon, H.I. Kim, Minireview: selective production of hydrogen peroxide as a clean oxidant over structurally tailored carbon nitride photocatalysts, *Catal. Today* 335 (2019) 55–64.
- A.T. Murray, S. Voskian, M. Schreier, T.A. Hatton, Y. Surendranath, Electrosynthesis of hydrogen peroxide by phase-transfer catalysis, *Joule* 3 (2019) 2942–2954.
- Y. Kofuji, Y. Isobe, Y. Shiraishi, H. Sakamoto, S. Tanaka, S. Ichikawa, T. Hirai, Carbon nitride-aromatic diimide-graphene nanohybrids: metal-free photocatalysts for solar-to-hydrogen peroxide energy conversion with 0.2% efficiency, *J. Am. Chem. Soc.* 138 (2016) 10019–10025.
- C. Chu, Q. Zhu, Z. Pan, S. Gupta, D. Huang, Y. Du, S. Weon, Y. Wu, C. Muhich, E. Stavitski, K. Domen, J.H. Kim, Spatially separating redox centers on 2D carbon nitride with cobalt single atom for photocatalytic  $\text{H}_2\text{O}_2$  production, *Proc. Natl. Acad. Sci. USA* 117 (2020) 6376–6382.
- H.B. Yang, J. Miao, S.-F. Hung, J. Chen, H.B. Tao, X. Wang, L. Zhang, R. Chen, J. Gao, H.M. Chen, L. Dai, B. Liu, Identification of catalytic sites for oxygen reduction and oxygen evolution in N-doped graphene materials: development of highly efficient metal-free bifunctional electrocatalyst, *Sci. Adv.* 2 (2016), e1501122.
- G.H. Moon, W. Kim, A.D. Bokare, N.E. Sung, W. Choi, Solar production of  $\text{H}_2\text{O}_2$  on reduced graphene oxide-TiO<sub>2</sub> hybrid photocatalysts consisting of earth-abundant elements only, *Energy Environ. Sci.* 7 (2014) 4023–4028.
- X.C. Wang, K. Maeda, A. Thomas, K. Takanabe, G. Xin, J.M. Carlsson, K. Domen, M. Antonietti, A metal-free polymeric photocatalyst for hydrogen production from water under visible light, *Nat. Mater.* 8 (2009) 76–80.
- Y. Wang, S.Z.F. Phua, G. Dong, X. Liu, B. He, Q. Zhai, Y. Li, C. Zheng, H. Quan, Z. Li, Y. Zhao, Structure tuning of polymeric carbon nitride for solar energy conversion: from nano to molecular scale, *Chem* 5 (2019) 2775–2813.
- L. Zhou, J.R. Feng, B.C. Qiu, Y. Zhou, J.Y. Lei, M.Y. Xing, L.Z. Wang, Y.B. Zhou, Y. D. Liu, J.L. Zhang, Ultrathin g-C<sub>3</sub>N<sub>4</sub> nanosheet with hierarchical pores and desirable energy band for highly efficient  $\text{H}_2\text{O}_2$  production, *Appl. Catal. B Environ.* 267 (2020), 118396.
- Z. Wei, M. Liu, Z. Zhang, W. Yao, H. Tan, Y. Zhu, Efficient visible-light-driven selective oxygen reduction to hydrogen peroxide by oxygen-enriched graphitic carbon nitride polymers, *Energy Environ. Sci.* 11 (2018) 2581–2589.
- P. Zhang, Y.W. Tong, Y. Liu, J.J.M. Vequizo, H.W. Sun, C. Yang, A. Yamakata, F. T. Fan, W. Lin, X.C. Wang, W. Choi, Heteroatom dopants-promoted two-electron O<sub>2</sub> reduction for photocatalytic production of  $\text{H}_2\text{O}_2$  on polymeric carbon nitride, *Angew. Chem. Int. Ed.* 59 (2020) 2–11.
- X.K. Zeng, Y. Liu, Y. Kang, Q.Y. Li, Y. Xia, Y.L. Zhu, H.L. Hou, M.H. Uddin, T. R. Gengenbach, D.H. Xia, C.H. Sun, D.T. McCarthy, A. Deletic, J.G. Yu, X.W. Zhang, Simultaneously tuning charge separation and oxygen reduction pathway on graphitic carbon nitride by polyethylenimine for boosted photocatalytic hydrogen peroxide production, *ACS Catal.* 10 (2020) 3697–3706.
- Y. Yang, G. Zeng, D. Huang, C. Zhang, D. He, C. Zhou, W. Wang, W. Xiong, X. Li, B. Li, W. Dong, Y. Zhou, Molecular engineering of polymeric carbon nitride for highly efficient photocatalytic oxytetracycline degradation and  $\text{H}_2\text{O}_2$  production, *Appl. Catal. B Environ.* 272 (2020), 118970.
- S. Zhao, T. Guo, X. Li, T.G. Xu, B. Yang, X. Zhao, Carbon nanotubes covalent combined with graphitic carbon nitride for photocatalytic hydrogen peroxide production under visible light, *Appl. Catal. B Environ.* 224 (2018) 725–732.
- Z. Yun, C. Yilin, G. Bifen, L. Bizhou, W. Xinchun, Black phosphorus and carbon nitride hybrid photocatalysts for photoredox reactions, *Adv. Funct. Mater.* 30 (2020), 2002021.
- Y. Shiraishi, Y. Kofuji, H. Sakamoto, S. Tanaka, S. Ichikawa, T. Hirai, Effects of surface defects on photocatalytic  $\text{H}_2\text{O}_2$  production by mesoporous graphitic carbon nitride under visible light irradiation, *ACS Catal.* 5 (2015) 3058–3066.
- L. Shi, L.Q. Yang, W. Zhou, Y.Y. Liu, L.S. Yin, X. Hai, H. Song, J.H. Ye, Photoassisted construction of holey defective g-C<sub>3</sub>N<sub>4</sub> photocatalysts for efficient visible-light-driven  $\text{H}_2\text{O}_2$  production, *Small* 14 (2018), 1703142.
- Y. Xie, Y.X. Li, Z.H. Huang, J.Y. Zhang, X.F. Jia, X.S. Wang, J.H. Ye, Two types of cooperative nitrogen vacancies in polymeric carbon nitride for efficient solar-driven  $\text{H}_2\text{O}_2$  evolution, *Appl. Catal. B Environ.* 265 (2020), 118581.
- H.J. Yu, R. Shi, Y.X. Zhao, T. Bian, Y.F. Zhao, C. Zhou, G.I.N. Waterhouse, L.Z. Wu, C.H. Tung, T.R. Zhang, Alkali-assisted synthesis of nitrogen deficient graphitic carbon nitride with tunable band structures for efficient visible-light-driven hydrogen evolution, *Adv. Mater.* 29 (2017), 1605148.
- Y. Wang, D. Meng, X. Zhao, Visible-light-driven  $\text{H}_2\text{O}_2$  production from O<sub>2</sub> reduction with nitrogen vacancy-rich and porous graphitic carbon nitride, *Appl. Catal. B Environ.* 273 (2020), 119064.
- S. Li, G. Dong, R. Hailili, L. Yang, Y. Li, F. Wang, Y. Zeng, C. Wang, Effective photocatalytic  $\text{H}_2\text{O}_2$  production under visible light irradiation at g-C<sub>3</sub>N<sub>4</sub> modulated by carbon vacancies, *Appl. Catal. B Environ.* 190 (2016) 26–35.
- C. Lv, Y.M. Qian, C.S. Yan, Y. Ding, Y.Y. Liu, G. Chen, G.H. Yu, Defect engineering metal-free polymeric carbon nitride electrocatalyst for effective nitrogen fixation under ambient conditions, *Angew. Chem. Int. Ed.* 57 (2018) 10246–10250.
- L.-L. Liu, F. Chen, J.-H. Wu, W.-W. Li, J.-J. Chen, H.-Q. Yu, Fine tuning of phosphorus active sites on g-C<sub>3</sub>N<sub>4</sub> nanosheets for enhanced photocatalytic decontamination, *J. Mater. Chem. A* 9 (2021) 10933–10944.
- Y. Yang, C. Zhang, D. Huang, G. Zeng, J. Huang, C. Lai, C. Zhou, W. Wang, H. Guo, W. Xue, R. Deng, M. Cheng, W. Xiong, Boron nitride quantum dots decorated ultrathin porous g-C<sub>3</sub>N<sub>4</sub>: intensified exciton dissociation and charge transfer for promoting visible-light-driven molecular oxygen activation, *Appl. Catal. B Environ.* 245 (2019) 87–99.
- Z. Fang, Y. Bai, L. Li, D. Li, Y. Huang, R. Chen, W. Fan, W. Shi, In situ constructing intramolecular ternary homojunction of carbon nitride for efficient photoinduced molecular oxygen activation and hydrogen evolution, *Nano Energy* 75 (2020), 104865.

- [31] Z. Qin, Z. Huang, M. Wang, D. Liu, Y. Chen, L. Guo, Synergistic effect of quantum confinement and site-selective doping in polymeric carbon nitride towards overall water splitting, *Appl. Catal. B Environ.* 261 (2020), 118211.
- [32] I. Krivtsov, D. Mitoraj, C. Adler, M. Ilkaeva, M. Sardo, L. Mafra, C. Neumann, A. Turchanin, C. Li, B. Dietzek, R. Leiter, J. Biskupek, U. Kaiser, C. Im, B. Kirchhoff, T. Jacob, R. Beranek, Water-soluble polymeric carbon nitride colloidal nanoparticles for highly selective quasi-homogeneous photocatalysis, *Angew. Chem. Int. Ed.* 59 (2020) 487–495.
- [33] F. Chen, L.-L. Liu, J.-J. Chen, W.-W. Li, Y.-P. Chen, Y.-J. Zhang, J.-H. Wu, S.-C. Mei, Q. Yang, H.-Q. Yu, Efficient decontamination of organic pollutants under high salinity conditions by a nonradical peroxymonosulfate activation system, *Water Res.* 191 (2021), 116799.
- [34] T.-P. André, J.S. Maria, G.S. Cláudia, L.F. Joaquim, M.T.S. Adrián, Metal-free carbon nitride photocatalysis with in situ hydrogen peroxide generation for the degradation of aromatic compounds, *Appl. Catal. B Environ.* 252 (2019) 128–137.
- [35] H. Yang, Y. Zhou, Y. Wang, S. Hu, B. Wang, Q. Liao, H. Li, J. Bao, G. Ge, S. Jia, Three-dimensional flower-like phosphorus-doped g-C<sub>3</sub>N<sub>4</sub> with a high surface area for visible-light photocatalytic hydrogen evolution, *J. Mater. Chem. A* 6 (2018) 16485–16494.
- [36] P. Zhang, D. Sun, A. Cho, S. Weon, S. Lee, J. Lee, J.-W. Han, D.-P. Kim, W. Choi, Modified carbon nitride nanozyme as bifunctional glucose oxidase-peroxidase for metal-free bioinspired cascade photocatalysis, *Nat. Commun.* 10 (2019) 940.
- [37] M. Wu, J. Zhang, B.-B. He, H.-W. Wang, R. Wang, Y.-S. Gong, In-situ construction of coral-like porous P-doped g-C<sub>3</sub>N<sub>4</sub> tubes with hybrid 1D/2D architecture and high efficient photocatalytic hydrogen evolution, *Appl. Catal. B Environ.* 241 (2019) 159–166.
- [38] J. Ran, W. Guo, H. Wang, B. Zhu, J. Yu, S.-Z. Qiao, Metal-free 2D/2D phosphorene/g-C<sub>3</sub>N<sub>4</sub> van der Waals heterojunction for highly enhanced visible-light photocatalytic H<sub>2</sub> production, *Adv. Mater.* 30 (2018), 1800128.
- [39] W. Che, W. Cheng, T. Yao, F. Tang, W. Liu, H. Su, Y. Huang, Q. Liu, J. Liu, F. Hu, Z. Pan, Z. Sun, S. Wei, Fast photoelectron transfer in (C<sub>ring</sub>)-C<sub>3</sub>N<sub>4</sub> plane heterostructural nanosheets for overall water splitting, *J. Am. Chem. Soc.* 139 (2017) 3021–3026.
- [40] N. Meng, J. Ren, Y. Liu, Y. Huang, T. Petit, B. Zhang, Engineering oxygen-containing and amino groups into two-dimensional atomically-thin porous polymeric carbon nitrogen for enhanced photocatalytic hydrogen production, *Energy Environ. Sci.* 11 (2018) 566–571.
- [41] D. Zhao, C.-L. Dong, B. Wang, C. Chen, Y.-C. Huang, Z. Diao, S. Li, L. Guo, S. Shen, Synergy of dopants and defects in graphitic carbon nitride with exceptionally modulated band structures for efficient photocatalytic oxygen evolution, *Adv. Mater.* 31 (2019), 1903545.
- [42] G.P. Mane, S.N. Talapaneni, K.S. Lakhi, H. Ilbeygi, U. Ravon, K. Al-Bahily, T. Mori, D.H. Park, A. Vinu, Highly ordered nitrogen-rich mesoporous carbon nitrides and their superior performance for sensing and photocatalytic hydrogen generation, *Angew. Chem. Int. Ed.* 56 (2017) 8481–8485.
- [43] Z. Mo, X. Zhu, Z. Jiang, Y. Song, D. Liu, H. Li, X. Yang, Y. She, Y. Lei, S. Yuan, H. Li, L. Song, Q. Yan, H. Xu, Porous nitrogen-rich g-C<sub>3</sub>N<sub>4</sub> nanotubes for efficient photocatalytic CO<sub>2</sub> reduction, *Appl. Catal. B Environ.* 256 (2019), 117854.
- [44] Z. Jingzhen, Y. Chunyang, L. Junyu, Z. Yongfeng, Z. Baoxue, H. Yun Hang, L. Mingce, Modulation of Lewis acidic-basic sites for efficient photocatalytic H<sub>2</sub>O<sub>2</sub> production over potassium intercalated tri-s-triazine materials, *Appl. Catal. B Environ.* 277 (2020), 119225.
- [45] F. Chen, L.-L. Liu, Y.-J. Zhang, J.-H. Wu, G.-X. Huang, Q. Yang, J.-J. Chen, H.-Q. Yu, Enhanced full solar spectrum photocatalysis by nitrogen-doped graphene quantum dots decorated BiO<sub>2-x</sub> nanosheets: ultrafast charge transfer and molecular oxygen activation, *Appl. Catal. B Environ.* 277 (2020), 119218.
- [46] Z. Teng, N. Yang, H. Lv, S. Wang, M. Hu, C. Wang, D. Wang, G. Wang, Edge-functionalized g-C<sub>3</sub>N<sub>4</sub> nanosheets as a highly efficient metal-free photocatalyst for safe drinking water, *Chem* 5 (2019) 664–680.
- [47] M. Bellardita, E.I. García-López, G. Marci, I. Krivtsov, J.R. García, L. Palmisano, Selective photocatalytic oxidation of aromatic alcohols in water by using P-doped g-C<sub>3</sub>N<sub>4</sub>, *Appl. Catal. B Environ.* 220 (2018) 222–233.
- [48] K. Satoshi, J. Jieun, S. Tomoyoshi, F. Shunichi, Production of hydrogen peroxide as a sustainable solar fuel from water and dioxygen, *Energy Environ. Sci.* 6 (2013) 3756–3764.
- [49] F. Chen, G.-X. Huang, F.-B. Yao, Q. Yang, Y.-M. Zheng, Q.-B. Zhao, H.-Q. Yu, Catalytic degradation of ciprofloxacin by a visible-light-assisted peroxymonosulfate activation system: performance and mechanism, *Water Res.* 173 (2020), 115559.
- [50] K. Gong, F. Du, Z. Xia, M. Durstock, L. Dai, Nitrogen-doped carbon nanotube arrays with high electrocatalytic activity for oxygen reduction, *Science* 323 (2009) 760–764.